Direct Active and Reactive Power Control of DFIG for Wind Energy Generation

Lie Xu, *Senior Member, IEEE*, and Phillip Cartwright

***Abstract*—This paper presents a new direct power control (DPC) strategy for a doubly fed induction generator (DFIG)-based wind energy generation system. The strategy is based on the direct control of stator active and reactive power by selecting appropriate voltage vectors on the rotor side. It is found that the initial rotor flux has no impact on the changes of the stator active and reactive power. The proposed method only utilizes the estimated stator flux so as to remove the difficulties associated with rotor flux estimation. The principles of this method are described in detail in this paper. The only machine parameter required by the proposed DPC method is the stator resistance whose impact on the system performance is found to be negligible. Simulation results on a 2 MW DFIG system are provided to demonstrate the effectiveness and robustness of the proposed control strategy during variations of active and reactive power, rotor speed, machine parameters, and converter dc link voltage.**

***Index Terms*—Direct power control (DPC), doubly fed induction generator (DFIG), direct torque control, voltage source converter, voltage vector.**

NOMENCLATURE

$\boldsymbol{V}_{\rm s}, \boldsymbol{V}_{\rm r}$	Stator, rotor voltage vectors.
$\boldsymbol{I}_{\rm s}, \boldsymbol{I}_{\rm r}$	Stator, rotor current vectors.
$i_{\rm sa}, i_{\rm sb}, i_{\rm sc}$	Stator three-phase currents.
$i_{\rm ra}, i_{\rm rb}, i_{rc}$	Rotor three-phase currents.
$\omega_1, \omega_{\rm r}$	Stator, rotor angular frequency.
$P_{\rm s}, Q_{\rm s}$	Stator active and reactive power.
$L_{\rm m}$	Mutual inductance.
$L_{\sigma{\rm s}}, L_{\sigma{\rm r}}$	Stator, rotor leakage inductance.
$L_{\rm s}, L_{\rm r}$	Stator, rotor self inductance.
$R_{\rm s}, R_{\rm r}$	Stator, rotor resistance.
$\psi_{\rm s}, \psi_{\rm r}$	Stator, rotor flux linkage vectors.
$\theta_{\rm s}, \theta_{\rm r}$	Stator, rotor flux angles in the rotor frame.
θ	Phase angle between the rotor and stator flux vectors.
$S_{\rm p}, S_{\rm q}$	Active and reactive power states.
p	Machine pole pairs.
Superscripts	
s	Stationary reference frame.
r	Rotor reference frame.
Subscripts	
α, β	α–β axis.
s, r	Stator, rotor.

Manuscript received June 27, 2005; revised October 24, 2005. Paper no. TEC-00204-2005.

L. Xu is with the School of Electronics, Electrical Engineering and Computer Science, Queen's University of Belfast, Belfast BT7 1NN, U.K. (e-mail: l.xu@ee.qub.ac.uk).

P. Cartwright was with the AREVA T&D Technology Centre, Stafford ST17 4LK, U.K. He is now with Rolls-Royce plc, Derby DE24 8BJ, U.K. (e-mail: phill.cartwright@rolls-royce.com).

Digital Object Identifier 10.1109/TEC.2006.875472

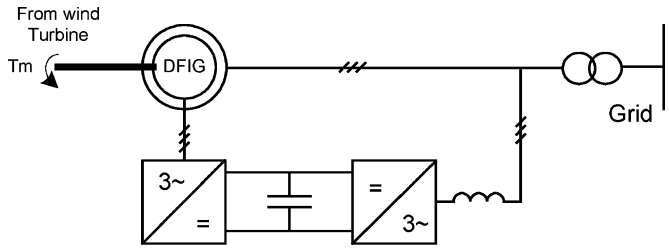

Fig. 1. Schematic diagram of DFIG-based wind generation systems.

I. INTRODUCTION

DUE to the increasing concern about CO_2 emissions, renewable energy systems and especially wind energy generation have attracted great interests in recent years. Large wind farms have been installed or planned around the world and the power ratings of the wind turbines are increasing. For many wind farms, wind turbines based on the doubly fed induction generator (DFIG) technology with converters rated at about 25%–30% of the generator rating are used. Compared to wind turbines using fixed speed induction generators, DFIG-based wind turbines offer several advantages including variable speed operation, and four-quadrant active and reactive power capabilities. Such system also results in lower converter costs and lower power losses compared to a system based on a fully fed synchronous generator with full-rated converter. A schematic diagram of a DFIG-based wind energy generation system is shown in Fig. 1.

Conventional design of DFIG control systems is based on rotor current vector control with d–q decoupling [1]–[3]. The control system is usually defined in the synchronous d–q frame fixed to either the stator voltage [1], [2] or the stator flux [3] and it involves relatively complex transformation of voltages, currents and control outputs among the stationary, the rotor and the synchronous reference frames. This conventional method requires accurate information of machine parameters such as stator, rotor resistance and inductance, and mutual inductance, etc. Thus, the performance is degraded when the actual machine parameters differ from those values used in the control system. In addition, the rotor current controllers need to be carefully tuned to ensure system stability and adequate response within the whole operating range.

Direct torque control (DTC) of induction machine drives was developed in the mid 1980s [4], [5]. The DTC method controls the machine torque directly by selecting appropriate voltage vectors using the stator flux and torque information. The stator flux is usually calculated by integrating the stator voltage. One of the main problems associated with the basic DTC scheme is that its performance deteriorates during starting and

very-low-speed operation. This is largely due to the fact that the method repeatedly selects zero voltage vectors at low speed resulting in flux level reduction owing to the stator resistance drop [6]. Many effects have been proposed to address this problem such as using a dither signal [7], a modified switching table in order to apply all the available voltage vectors in appropriate sequence [8], or predictive techniques [9]. Apart from induction machines, DTC has also been applied to control permanent magnet synchronous motors [10] and switched reluctance motors [11].

Based on the principles of DTC for electrical machine drives, direct power control (DPC) for three-phase PWM rectifiers was proposed in [12]–[14]. In [12], the converter switching states were selected from an optimal switching table based on the instantaneous errors between the reference and estimated values of active and reactive power, and the angular position of the estimated converter terminal voltage vector. The converter terminal voltage was estimated using the dc link voltage and converter switching states. Thus, no voltage sensor was required. In [13], instead of using the angular position of the voltage vector proposed in [12], the position of the virtual flux, which is the integration of the converter output voltage, was used. A phase-locked loop (PLL) was also proposed for detecting the position of the virtual flux to provide improved system performance under distorted or unbalanced voltage supply. In [14], output regulation subspace (ORS) was used to modify the original voltage vector position for selecting the switching states to improve the system performance, especially under distorted or unbalanced supply conditions.

In [15], DTC was used to control a DFIG. The converter is connected to the rotor side within a DFIG system, and hence the rotor flux was estimated. The rotor flux reference was calculated based on the required operating power factor. A switching vector was then selected from the optimal switching table based on the estimated rotor flux position, the torque and the rotor flux errors. Since the frequency of the rotor supply, which is equal to the DFIG slip frequency, could become very low, the rotor flux estimation method presents difficulties and its accuracy is significantly affected by the machine parameter variations. Furthermore, the calculation of the rotor flux reference according to the required power factor also requires the reference of actual parameters and therefore has the same problem.

This paper proposes a new DPC control strategy for a DFIG-based wind energy generation system. The control method is based on the stator flux and the only machine parameter required is the stator resistance. Simulation results on a 2 MW DFIG generation system are presented to demonstrate the performance of the proposed control strategy during variations of rotor speed, active and reactive power, machine parameter, and converter dc link voltage.

II. Dynamic Behavior of a DFIG in the Rotor Reference Frame

The equivalent circuit of a DFIG expressed in the rotor reference frame (α_r–β_r frame) rotating at a speed of ω_r is shown in Fig. 2. As it is shown, in the rotor reference frame, the stator and rotor flux linkage vectors can be expressed as

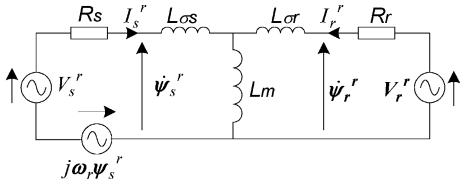

Fig. 2. Equivalent circuit of a DFIG in the rotor reference frame.

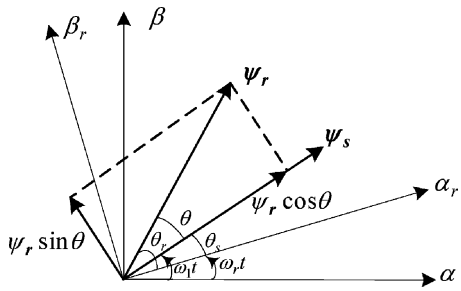

Fig. 3. Relation of stator and rotor flux linkage vectors in stationary and rotor reference frames.

$$\psi_{\mathrm{s}}^{\mathrm{r}} = L_{\mathrm{s}}\boldsymbol{I}_{\mathrm{s}}^{\mathrm{r}} + L_{\mathrm{m}}\boldsymbol{I}_{\mathrm{r}}^{\mathrm{r}}$$
$$\psi_{\mathrm{r}}^{\mathrm{r}} = L_{\mathrm{r}}\boldsymbol{I}_{\mathrm{r}}^{\mathrm{r}} + L_{\mathrm{m}}\boldsymbol{I}_{\mathrm{s}}^{\mathrm{r}}. \tag{1}$$

According to (1), stator current can be calculated as

$$\boldsymbol{I}_{\mathrm{s}}^{\mathrm{r}} = \frac{L_{\mathrm{r}}\psi_{\mathrm{s}}^{\mathrm{r}} - L_{\mathrm{m}}\psi_{\mathrm{r}}^{\mathrm{r}}}{L_{\mathrm{s}}L_{\mathrm{r}} - L_{\mathrm{m}}^2} = \frac{\psi_{\mathrm{s}}^{\mathrm{r}}}{\sigma L_{\mathrm{s}}} - \frac{L_{\mathrm{m}}\psi_{\mathrm{r}}^{\mathrm{r}}}{\sigma L_{\mathrm{s}}L_{\mathrm{r}}} \tag{2}$$

where $\sigma = (L_{\mathrm{s}}L_{\mathrm{r}} - L_{\mathrm{m}}^2)/L_{\mathrm{s}}L_{\mathrm{r}}$ is the leakage factor.

From Fig. 2, the stator voltage vector is expressed as

$$\boldsymbol{V}_{\mathrm{s}}^{\mathrm{r}} = R_{\mathrm{s}}\boldsymbol{I}_{\mathrm{s}}^{\mathrm{r}} + \dot{\psi}_{\mathrm{s}}^{\mathrm{r}} + j\omega_{\mathrm{r}}\psi_{\mathrm{s}}^{\mathrm{r}}. \tag{3}$$

Based on Fig. 2 and (3), the stator active power input from the network can be expressed as

$$P_{\mathrm{s}} = \frac{3}{2}\boldsymbol{V}_{\mathrm{s}}^{\mathrm{r}} \cdot \boldsymbol{I}_{\mathrm{s}}^{\mathrm{r}} = \frac{3}{2}\left(R_{\mathrm{s}}\boldsymbol{I}_{\mathrm{s}}^{\mathrm{r}} + \dot{\psi}_{\mathrm{s}}^{\mathrm{r}} + j\omega_{\mathrm{r}}\psi_{\mathrm{s}}^{\mathrm{r}}\right) \cdot \boldsymbol{I}_{\mathrm{s}}^{\mathrm{r}}. \tag{4}$$

Neglecting the stator copper loss, (4) becomes

$$P_{\mathrm{s}} = \frac{3}{2}\left(\dot{\psi}_{\mathrm{s}}^{\mathrm{r}} + j\omega_{\mathrm{r}}\psi_{\mathrm{s}}^{\mathrm{r}}\right) \cdot \boldsymbol{I}_{\mathrm{s}}^{\mathrm{r}}. \tag{5}$$

Similarly, the stator reactive power output to the network is given by

$$Q_{\mathrm{s}} = -\frac{3}{2}\boldsymbol{V}_{\mathrm{s}}^{\mathrm{r}} \times \boldsymbol{I}_{\mathrm{s}}^{\mathrm{r}} = -\frac{3}{2}\left(\dot{\psi}_{\mathrm{s}}^{\mathrm{r}} + j\omega_{\mathrm{r}}\psi_{\mathrm{s}}^{\mathrm{r}}\right) \times \boldsymbol{I}_{\mathrm{s}}^{\mathrm{r}}. \tag{6}$$

The relationship between the stator and rotor flux in the stationary α–β and rotor α_{r}–β_{r} reference frames is shown in Fig. 3. As shown, the stator and rotor flux in the rotor α_{r}–β_{r} frame can be expressed as

$$\psi_{\mathrm{s}}^{\mathrm{r}} = |\psi_{\mathrm{s}}^{\mathrm{r}}| \cdot e^{j\theta_{\mathrm{s}}} \tag{7a}$$
$$\psi_{\mathrm{r}}^{\mathrm{r}} = |\psi_{\mathrm{r}}^{\mathrm{r}}| \cdot e^{j\theta_{\mathrm{r}}} \tag{7b}$$

while the transformation of the stator flux in the two reference frames is given by

$$\psi_{\mathrm{s}}^{\mathrm{r}} = \psi_{\mathrm{s}}^{\mathrm{s}} \cdot e^{-j\omega_{\mathrm{r}}t}. \tag{7c}$$

According to Fig. 3, the following relation also exists

$$\dot{\theta}_{\mathrm{s}} = \omega_1 - \omega_{\mathrm{r}}. \tag{8}$$

In the stationary reference frame, the stator flux can be expressed as [4]

$$\psi_{\mathrm{s}}^{\mathrm{s}} = \int \left(\boldsymbol{V}_{\mathrm{s}}^{\mathrm{s}} - R_{\mathrm{s}}\boldsymbol{I}_{\mathrm{s}}^{\mathrm{s}}\right) dt. \tag{9}$$

Neglecting the stator resistance and assuming the ac network connected to the stator is well balanced and the rotor speed does not change within the sampling period considered which is usually true due to the relatively large inertia of the wind turbine, then from (7c)

$$\left|\psi_{\mathrm{s}}^{\mathrm{r}}\right| = \left|\psi_{\mathrm{s}}^{\mathrm{s}} e^{-j\omega_{\mathrm{r}}t}\right| = \left|\int \boldsymbol{V}_{\mathrm{s}}^{\mathrm{s}}\, dt\right| = \text{constant}$$

$$\frac{d\left|\psi_{\mathrm{s}}^{\mathrm{r}}\right|}{dt} = 0. \tag{10}$$

Differentiating (7a) and taking into account (8) and (10) yield

$$\dot{\psi}_{\mathrm{s}}^{\mathrm{r}} = \left|\psi_{\mathrm{s}}^{\mathrm{r}}\right| j\dot{\theta}_{\mathrm{s}} e^{j\theta_{\mathrm{s}}} = j\left(\omega_1 - \omega_{\mathrm{r}}\right)\psi_{\mathrm{s}}^{\mathrm{r}}. \tag{11}$$

As shown in Appendix A, substituting (2) and (11) into (5) and (6) results in the stator active power input and reactive power output as

$$P_{\mathrm{s}} = -\frac{3}{2}\frac{L_{\mathrm{m}}}{\sigma L_{\mathrm{s}} L_{\mathrm{r}}}\omega_1 \left|\psi_{\mathrm{s}}^{\mathrm{r}}\right| \left|\psi_{\mathrm{r}}^{\mathrm{r}}\right| \sin\theta \tag{12}$$

$$Q_{\mathrm{s}} = \frac{3}{2}\frac{\omega_1}{\sigma L_{\mathrm{s}}}\left|\psi_{\mathrm{s}}^{\mathrm{r}}\right| \left(\frac{L_{\mathrm{m}}}{L_{\mathrm{r}}}\left|\psi_{\mathrm{r}}^{\mathrm{r}}\right| \cos\theta - \left|\psi_{\mathrm{s}}^{\mathrm{r}}\right|\right) \tag{13}$$

where $\theta = \theta_{\mathrm{r}} - \theta_{\mathrm{s}}$ is the angle between the rotor and stator flux linkage vectors.

Differentiating (12) and (13) results in the following equations

$$\frac{dP_{\mathrm{s}}}{dt} = -\frac{3}{2}\frac{L_{\mathrm{m}}}{\sigma L_{\mathrm{s}} L_{\mathrm{r}}}\omega_1 \left|\psi_{\mathrm{s}}^{\mathrm{r}}\right| \frac{d\left(\left|\psi_{\mathrm{r}}^{\mathrm{r}}\right| \sin\theta\right)}{dt}$$

$$\frac{dQ_{\mathrm{s}}}{dt} = \frac{3}{2}\frac{L_{\mathrm{m}}}{\sigma L_{\mathrm{s}} L_{\mathrm{r}}}\omega_1 \left|\psi_{\mathrm{s}}^{\mathrm{r}}\right| \frac{d\left(\left|\psi_{\mathrm{r}}^{\mathrm{r}}\right| \cos\theta\right)}{dt}. \tag{14}$$

According to (14), it can be seen that fast active and reactive power changes can be achieved by changing $\left|\psi_{\mathrm{r}}^{\mathrm{r}}\right| \sin\theta$ and $\left|\psi_{\mathrm{r}}^{\mathrm{r}}\right| \cos\theta$, respectively. From Fig. 3, $\left|\psi_{\mathrm{r}}^{\mathrm{r}}\right| \sin\theta$ and $\left|\psi_{\mathrm{r}}^{\mathrm{r}}\right| \cos\theta$ represent the components of the rotor flux $\psi_{\mathrm{r}}^{\mathrm{r}}$ at the perpendicular and the same direction of the stator flux respectively. This indicates that, if the change of the rotor flux is at the stator flux direction, i.e., $\left|\psi_{\mathrm{r}}^{\mathrm{r}}\right| \cos\theta$ reactive power Q_{s} is changed. Alternatively, if the change of the rotor flux is at 90° to the stator flux direction, i.e., $\left|\psi_{\mathrm{r}}^{\mathrm{r}}\right| \sin\theta$ active power P_{s} is changed. The initial position of the rotor flux and its amplitude do not directly affect the active and reactive power changes.

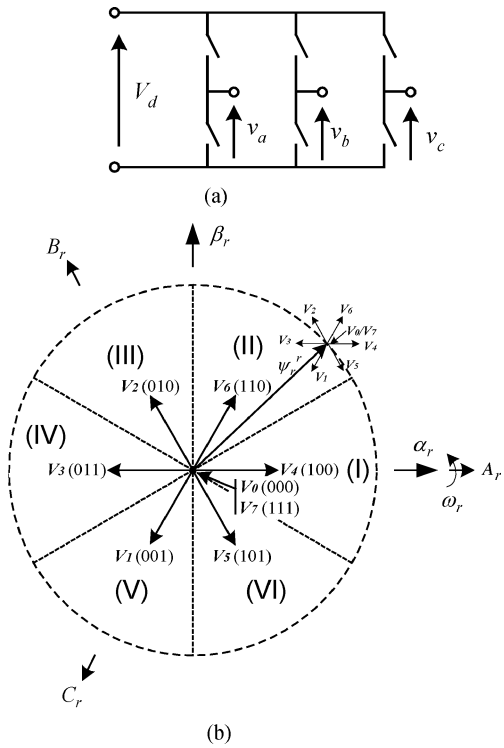

Fig. 4. (a) Two-level converter. (b) Voltage vectors and the control of flux using voltage vectors.

III. Rotor Flux Control Using Voltage Vectors

For a two-level converter shown in Fig. 4(a), each of the three-phase outputs v_{a}, v_{b}, and v_{c} can have two levels, i.e., $+V_{\mathrm{d}}$ and 0. The output three-phase voltages can be represented by a voltage vector and according to the output voltage levels of each phase, there are eight voltage vectors available [16], [17]. Fig. 4(b) shows these eight voltage vectors noted as $V_0(000)$–$V_7(111)$ where the binary numbers in the parentheses express the switching pattern in the phase sequence (a, b, c) and the subscript of $\boldsymbol{V}$ is the decimal expression of the binary number. "1" means the top switch is on and the output voltage is V_d while "0" means the bottom switch is on and the output voltage is zero. Among the eight voltage vectors, two are zero voltage vectors (V_0 and V_7) and six are active vectors $(V_1 - V_6)$.

As shown in Fig. 2, similar to the stator flux, the rotor flux of a DFIG in the rotor α_{r}–β_{r} frame can be expressed as

$$\frac{d\psi_{\mathrm{r}}^{\mathrm{r}}}{dt} = \boldsymbol{V}_{\mathrm{r}}^{\mathrm{r}} - R_{\mathrm{r}}\boldsymbol{I}_{\mathrm{r}}^{\mathrm{r}} \tag{15}$$

Neglecting the effect of rotor resistance R_{r}, (15) indicates that the variation of rotor flux is determined by the applied rotor voltage. The rotor flux moves at the direction of applied rotor voltage vector and its speed is proportional to the amplitude of the voltage vector applied. Therefore, by selecting appropriate voltage vectors, the movement of the rotor flux can be controlled. The selection of the voltage vector also depends on the location of the flux linkage and the α_{r}–β_{r} plane is divided into six regions (I–VI) as shown in Fig. 4.

IV. Direct Active and Reactive Power Control

A. Impact of Voltage Vectors on Active and Reactive Power

According to (15), Zero voltage vectors stall the movement of the rotor flux if the voltage drop across the rotor resistance is neglected. If the rotor flux stalls, there are

$$d\,|\psi_{\mathrm{r}}^{\mathrm{r}}|/dt = 0, \quad d\theta_{\mathrm{r}}/dt = 0. \tag{16}$$

Substituting (16) into (14) and taking into account $\theta = \theta_{\mathrm{r}} - \theta_{\mathrm{s}}$ yield

$$\begin{aligned}\frac{dP_{\mathrm{s}}}{dt} &= \frac{3}{2}\frac{L_{\mathrm{m}}}{\sigma L_{\mathrm{s}} L_{\mathrm{r}}}\omega_1\,|\psi_{\mathrm{s}}^{\mathrm{r}}|\,|\psi_{\mathrm{r}}^{\mathrm{r}}|\cos(\theta_{\mathrm{r}}-\theta_{\mathrm{s}})(\omega_1-\omega_{\mathrm{r}})\\ \frac{dQ_{\mathrm{s}}}{dt} &= \frac{3}{2}\frac{L_{\mathrm{m}}}{\sigma L_{\mathrm{s}} L_{\mathrm{r}}}\omega_1\,|\psi_{\mathrm{s}}^{\mathrm{r}}|\,|\psi_{\mathrm{r}}^{\mathrm{r}}|\sin(\theta_{\mathrm{r}}-\theta_{\mathrm{s}})(\omega_1-\omega_{\mathrm{r}}).\end{aligned} \tag{17}$$

Equation (17) indicates that the effect of zero space vectors on the active and reactive power largely depends on the sign of $(\omega_1 - \omega_{\mathrm{r}})$. Under normal generation mode, rotor flux always leads the stator flux, i.e., $\theta_{\mathrm{r}} > \theta_{\mathrm{s}}$. Therefore, for super-synchronous operation, i.e., rotor speed higher than stator speed $(\omega_{\mathrm{r}} > \omega_1)$, zero voltage vectors reduce the active power input and reactive power output and vice versa for sub-synchronous operation $(\omega_{\mathrm{r}} < \omega_1)$.

As described in the previous sections, an active voltage vector moves the rotor flux in the same direction as that of the voltage vector. If the stator flux position is known, the changes of $|\psi_{\mathrm{r}}^{\mathrm{r}}|\sin\theta$ and $|\psi_{\mathrm{r}}^{\mathrm{r}}|\cos\theta$ can be identified for each rotor voltage vector. Thus, according to (14), the impact of each voltage vector on active and reactive power in each 60° region can be calculated. Only the stator flux position is required as the initial rotor flux is irrelevant to the changes of the active and reactive power.

With a DFIG, the rotor flux can be calculated by integrating (15). However, as the rotor voltage has low fundamental frequency the use of integrators does not achieve satisfactory results. This is due to the factor that errors at very low frequency caused by the difference of the actual value of R_{r} and the one used in the calculation, can cause the integrators to saturate. Based on (1), an alternative method could be used

$$\psi_{\mathrm{r}}^{\mathrm{r}} = \frac{L_{\mathrm{m}}}{L_{\mathrm{s}}}\psi_{\mathrm{s}}^{\mathrm{r}} + \frac{L_{\mathrm{s}}L_{\mathrm{r}} - L_{\mathrm{m}}^2}{L_{\mathrm{s}}} I_{\mathrm{r}}^{\mathrm{r}}. \tag{18}$$

However, (18) requires the stator, the rotor and the mutual inductance and using this method may result in an accuracy which is significantly reduced when these inductance values used in the calculation deviate from their real values.

Since the proposed method only uses the stator flux, it removes the problems associated with the estimation of the rotor flux.

Thus, the effects of the eight voltage vectors on active and reactive power for each 60° region now can be identified and they are shown in Table I.

TABLE I
Effect of Voltage Vectors on Input Active and Output Reactive Power (↑= Increase; ↓= Decrease)

ψ_s^r region N		I	II	III	IV	V	VI
V_1 (001)	Ps	↑	↓/↑	↓	↓	↑/↓	↑
	Qs	↓	↓	↓	↑	↑	↑
V_2 (010)	Ps	↓	↓	↑/↓	↑	↑	↓/↑
	Qs	↓	↑	↓	↑	↓	↓
V_3 (011)	Ps	↓/↑	↓	↑	↑/↓	↑	↑
	Qs	↓	↓	↑	↑	↑	↓
V_4 (100)	Ps	↑/↓	↑	↑	↓/↑	↓	↓
	Qs	↑	↑	↓	↓	↓	↑
V_5 (101)	Ps	↑	↑	↓/↑	↓	↓	↑/↓
	Qs	↑	↓	↓	↓	↑	↑
V_6 (110)	Ps	↓	↑/↓	↑	↑	↓/↑	↓
	Qs	↑	↑	↑	↓	↓	↓

ψ_s^r region N			I -- VI
V_0/V_7 (000)/ (111)	$\omega_1>\omega_r$	Ps	↑
		Qs	↑
	$\omega_1<\omega_r$	Ps	↓
		Qs	↓

B. Stator Flux Estimation

In order to calculate the stator flux linkage vector in the rotor reference frame, its value in the stationary reference frame is estimated first. It is then transformed into the rotor α_{r}–β_{r} frame using the information of rotor position which, in practice, is normally obtained via a shaft encoder.

In the stationary reference frame, the stator flux linkage is estimated using the following equation:

$$\psi_{\mathrm{s}}^{\mathrm{s}} = \int (\boldsymbol{V}_{\mathrm{s}}^{\mathrm{s}} - R_{\mathrm{s}}\boldsymbol{I}_{\mathrm{s}}^{\mathrm{s}})dt \tag{19}$$

Since the stator voltage is relatively harmonic-free and its frequency is fixed, the above equation can provide an accurate estimation of the stator flux.

The stator flux linkage vector in the rotor reference frame is calculated according to (7c) also using the measured rotor position.

C. Direct Active and Reactive Power Control

In order to achieve high dynamic control of active and reactive power, the active and reactive power states and stator flux position are used to determine which voltage vector is applied. Two three-level hysteresis comparators are used to generate the respective active and reactive power states S_{p} and S_{q} as Fig. 5 shows.

As previously described, zero voltage vectors have different impact on active and reactive power for different operating rotor speeds. Due to the presence of rotor resistance, the impact of zero voltage vectors becomes more complicated especially when the rotor speed approaches the synchronous speed. Therefore, zero voltage vectors will not be used except when both active and reactive power states are zero.

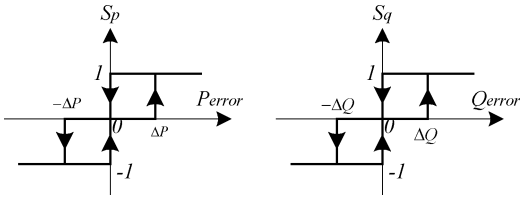

Fig. 5. Active and reactive power hysteresis control.

TABLE II
OPTIMAL SWITCHING TABLE

		I	II	III	IV	V	VI
Sq=1	Sp=1	101	100	110	010	011	001
	Sp=0	100	110	010	011	001	101
	Sp=-1	110	010	011	001	101	100
Sq=0	Sp=1	001	101	100	110	010	011
	Sp=0	111/ 000	111/ 000	111/ 000	111/ 000	111/ 000	111/ 000
	Sp=-1	010	011	001	101	100	110
Sq=-1	Sp=1	001	101	100	110	010	011
	Sp=0	011	001	101	100	110	010
	Sp=-1	010	011	001	101	100	110

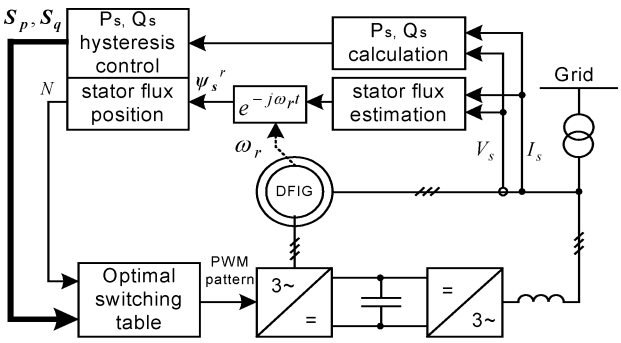

Fig. 6. Schematic diagram of the proposed DPC for a DFIG system.

Based on the above analysis, the optimal switching table is arranged and it is shown in Table II. The selection of the alternative two zero voltage vectors during $S_q = 0$ and $S_p = 0$ is used to reduce the switching frequency by switching only one phase leg. Fig. 6 shows the schematic diagram of the proposed DPC strategy.

As shown in Fig. 6, the three-phase ac voltages and currents of the stator are measured and transformed into the stationary α–β reference frame. The active and reactive power are calculated and the stator flux is then estimated. The rotor speed/position is measured and is used to transform the stator flux from the α–β frame to the rotor $\alpha_{\rm r}$–$\beta_{\rm r}$ frame. The calculated active and reactive power are compared to their reference values and $S_{\rm p}$ and $S_{\rm q}$ are generated. The two active and reactive power states are then fed to the optimal switching table together with the calculated stator flux position to obtain the appropriate switching states.

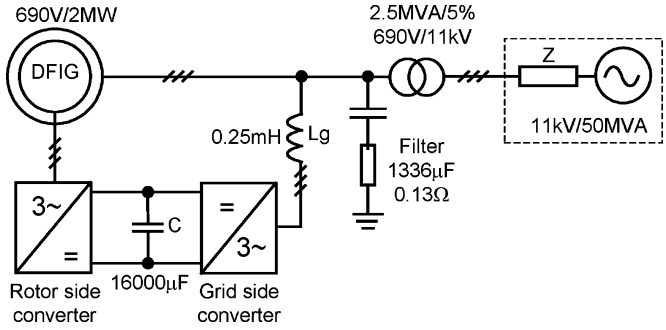

Fig. 7. Schematic diagram of the simulated system.

Finally, the optimal switching states are fed to the converter to provide the control required to reduce the power errors.

V. SIMULATION RESULTS

Simulation of the proposed control strategy for a DFIG-based generation system was carried out using PSCAD/EMTDC and Fig. 7 shows the schematic diagram of the system implemented. The DFIG is rated at 2 MW and its parameters are given in the Appendix B. The nominal dc link voltage is set at 1200 V and the dc capacitance is 16 000 μF. A simple RC filter is connected to the stator as shown in Fig. 7 to absorb the switching harmonics generated by the converters. The rotor side converter is used to control the DFIG stator active and reactive power based on the proposed DPC strategy. During simulation, the sampling frequency is 20 kHz and the bandwidths of the active and reactive power hysteresis controllers are set at $\pm 4\%$ of the rated generator power of 2 MW. The main objective of the grid side converter is to maintain a constant dc link voltage and it is controlled using a similar method as the dc voltage controller in a VSC Transmission system [18] and the shunt converter in an UPFC [19]. The switching frequency for the grid side converter is 1950 Hz and the series reactor is 0.25 mH.

The grid side converter is enabled first, such that the common dc link voltage is regulated. The DFIG stator is then energized with the rotor rotating at a set speed and the rotor side converter disabled. This process is not shown in the following results.

First, the DFIG was assumed to be in speed control, i.e., the rotor speed is set externally, as the large inertia of the wind turbine results in slow change of rotor speed. The rotor side converter was enabled at 0.2 s with the initial stator active and reactive power references being -2 MW and -0.66 Mvar, respectively ("$-$" refers to generating active power and absorbing reactive power). Simulations of various active and reactive power steps with constant rotor speed were carried out and the results are shown in Fig. 8 (A) and (B) for rotor speeds of 1.0 and 1.2 p.u., respectively, where the synchronous speed is defined as 1 unit. The active and reactive power references were step changed from -2 to -1 MW at 0.4 s and from -0.66 to $+0.66$ MVar at 0.6 s, respectively. The effectiveness of the proposed control strategy is clearly indicated in Fig. 8. The responses of both active and reactive power during step change of their references

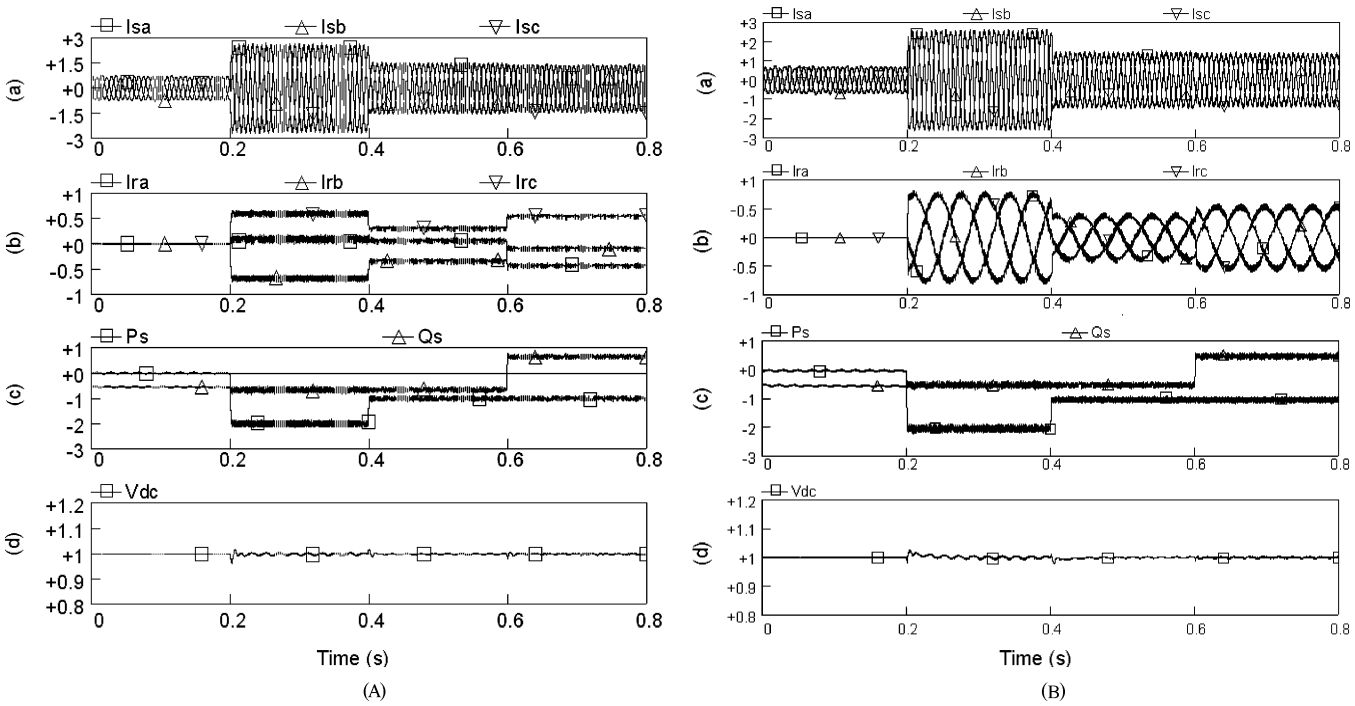

Fig. 8. Simulated results under various stator active and reactive power steps and constant rotor angular speed (A) 1.0 p.u., and (B) 1.2 p.u.: (a) Three-phase stator current (kA); (b) three-phase rotor current (kA); (c) stator active power input (MW) and reactive power output (MVar); (d) dc link voltage (p.u.).

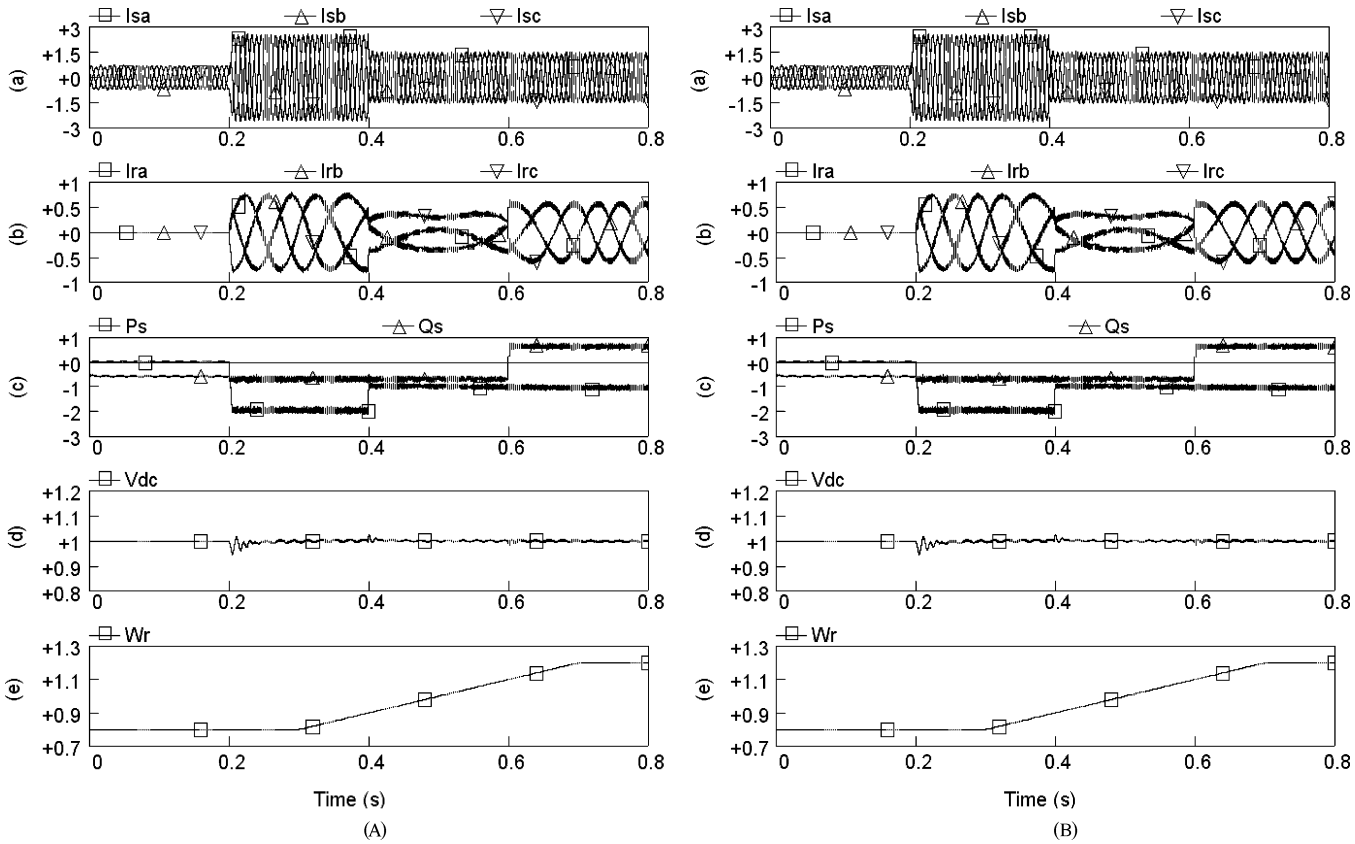

Fig. 9. Simulated results under various stator active and reactive power steps and rotor speed variation (A) without stator resistance error and (B) with 90% stator resistance error: (a) Three-phase stator current (kA); (b) three-phase rotor current (kA); (c) stator active power input (MW) and reactive power output (MVar); (d) dc link voltage (p.u.); (e) rotor speed (p.u.).

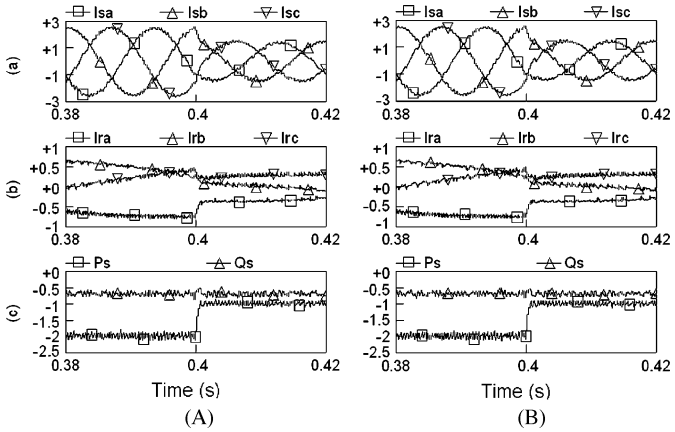

Fig. 10. Comparison of system responses with and without stator resistance error. (A) Without error. (B) With 90% error.

are within a few milliseconds. There is no over shoot of either the stator/rotor currents or the active/reactive power.

Simulations with various power steps and rotor speed variation have been carried out to further test the proposed control schemes. Fig. 9(A) shows the simulation results with the stator resistance used in the flux estimation matching the real value of the DFIG. As shown, during the period of 0.3–0.7 s, the rotor speed increases from 0.8 to 1.2 p.u. Various power steps are also applied, i.e., active and reactive power references are changed from -2 to -1 MW at 0.4 s and from -0.66 to $+0.66$ MVar at 0.6 s, respectively. Again the response of the system is satisfactory.

The robustness of the DPC strategy is studied using the error of the stator resistance whose value used in the stator flux observer shown in (19) is reduced to 10% of its real value. For the same operation conditions as those shown in Fig. 9(A), the simulated results are shown in Fig. 9(B). Comparing Fig. 9(A) with Fig. 9(B), there is hardly any difference and even with the large error of the stator resistance value used, the system maintains superb performance under both steady state and transient conditions. This is further proved in Fig. 10, which compares the response of the system at around 0.4 s with and without stator resistance error.

Further tests with the DFIG being in torque control, i.e., the speed is the result of stator/rotor voltage/current and the mechanical torque which is specified by external input to simulate the torque from the turbine. Fig. 11 shows the simulated results when the input mechanical torque step changed at 0.1 s from 0.3 to 1 p.u. The active power output reference from the DFIG is calculated from the optimal power-speed curve [1]. The lumped inertia constant of the system is set to a relatively low value in the study to reduce the simulation time. As can be seen, when the mechanical torque increases, the rotor speeds up and the active power generated by the DFIG according to the optimal operation curve also increases. The reactive power reference is changed from 0 to $+0.66$ MVar at 0.3 s. Fig. 11 clearly shows that the operation of the system is satisfactory during torque variation.

The robustness of the proposed DPC was also tested with converter dc voltage variation. This was achieved by degrading the

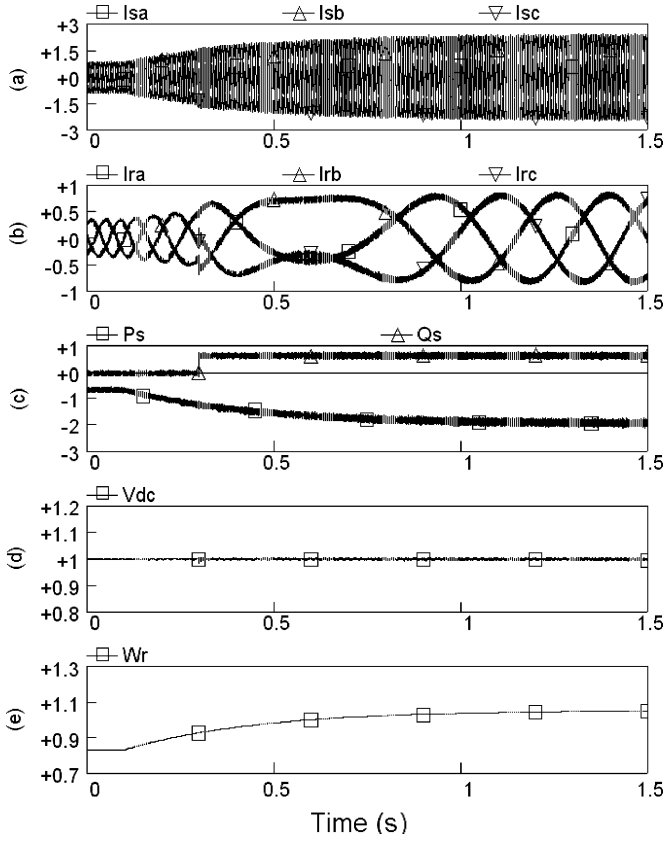

Fig. 11. Simulated results with step change of mechanical input torque at 0.1 s (from 0.3 to 1.0 p.u).

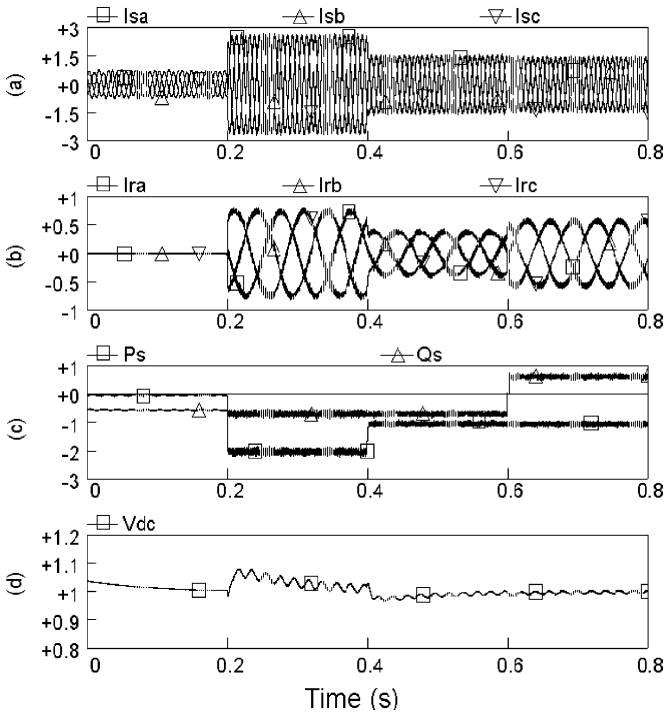

Fig. 12. Simulation results with imperfect dc link voltage [same operating condition as that shown in Fig. 8(B)].

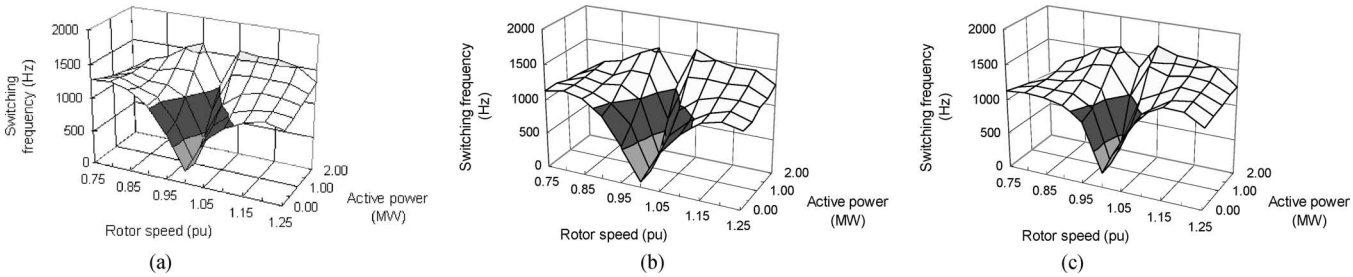

Fig. 13. Variation of converter switching frequency with active, reactive power, and rotor speed. (a) Q $= -0.66$ Mvar. (b) Q $= 0$. (c) Q $= +0.66$ Mvar.

performance of the grid side converter such that under transient conditions the dc voltage can vary significantly. The results are shown in Fig. 12 for the same operating condition as that shown in Fig. 8(B). Compared Fig. 12 with Fig. 8(B), it can be seen that the impact of dc voltage variation on both the dynamic and stead state performances of the DPC strategy is negligible.

In a practical system, a shaft encoder is normally used to obtain the rotor angle and this can be achieved to a very high accuracy. Further tests were carried out with induced rotor angle error equivalent to one pulse period of a 5000 pulses per revolution encoder, i.e., electric angle of 0.144° for a 4-pole DFIG. It showed that the impact of such angle error on the system performance is also negligible.

As the converter's switching states are determined by the stator active and reactive power errors and stator flux position, the converter average switching frequency is not fixed and could vary with the variations of operating conditions. The impacts of machine parameters, the machine operation conditions such as the rotor speed, the stator active and reactive power, and the hysteresis bands on the converter switching frequency is complicated and their relationship are highly nonlinear. The work is currently ongoing and the full results will be reported in the future. Fig. 13 shows the variations of converter switching frequency with active power, reactive power, and rotor speed. As can be seen, reactive power has little influence on the switching frequency. The impact of active power on converter switching frequency becomes significant only when the rotor speed approaches the synchronous speed. The development of DPC with constant switching frequency such as the approach adopted in [20] is also ongoing.

VI. Conclusion

A new direct active and reactive power control strategy for a DFIG system has been proposed in this paper. The method selects appropriate voltage vectors based on the stator flux position and active and reactive power errors. Thus, the difficulties associated with the rotor flux estimation are removed. The only machine parameter required by the DPC strategy is the stator resistance whose impact on the system performance is negligible. An optimal switching table has been derived and two three-level hysteresis comparators are used to determine the power errors. Simulation results presented confirm the effectiveness and robustness of the proposed DPC strategy during various operating conditions and variations of machine parameter and converter dc link voltage.

Appendix A

Stator Active Power Input and Reactive Power Output

Substituting (2) and (11) into (5) yields

$$\begin{aligned} P_{\rm s} &= \frac{3}{2}\left(\dot{\psi}_{\rm s}^{\rm r} + j\omega_{\rm r}\psi_{\rm s}^{\rm r}\right)\cdot \boldsymbol{I}_{\rm s}^{\rm r} \\ &= \frac{3}{2}\left[j(\omega_1-\omega_{\rm r})\psi_{\rm s}^{\rm r} + j\omega_{\rm r}\psi_{\rm s}^{\rm r}\right]\cdot\left(\frac{\psi_{\rm s}^{\rm r}}{\sigma L_{\rm s}} - \frac{L_{\rm m}\psi_{\rm r}^{\rm r}}{\sigma L_{\rm s}L_{\rm r}}\right) \\ &= \frac{3}{2}\left(j\omega_1\psi_{\rm s}^{\rm r}\right)\cdot\left(\frac{\psi_{\rm s}^{\rm r}}{\sigma L_{\rm s}} - \frac{L_{\rm m}\psi_{\rm r}^{\rm r}}{\sigma L_{\rm s}L_{\rm r}}\right) \\ &= -\frac{3}{2}\left[j\omega_1\psi_{\rm s}^{\rm r}\cdot\frac{L_{\rm m}\psi_{\rm r}^{\rm r}}{\sigma L_{\rm s}L_{\rm r}}\right] \\ &= -\frac{3}{2}\frac{L_{\rm m}}{\sigma L_{\rm s}L_{\rm r}}\omega_1\left(j\psi_{\rm s}^{\rm r}\cdot\psi_{\rm r}^{\rm r}\right) \end{aligned} \tag{A1}$$

According to Fig. 3, (7a) and (7b), the above equation can be expressed as

$$P_{\rm s} = -\frac{3}{2}\frac{L_{\rm m}}{\sigma L_{\rm s}L_{\rm r}}\omega_1\left|\psi_{\rm s}^{\rm r}\right|\left|\psi_{\rm r}^{\rm r}\right|\sin\theta \tag{A2}$$

where $\theta = \theta_{\rm r} - \theta_{\rm s}$ is the angle between the rotor and stator flux linkage vectors as illustrated in Fig. 3.

Similarly, substituting (2) and (11) into (6) results in the DFIG output reactive power as

$$\begin{aligned} Q_{\rm s} &= -\frac{3}{2}\left(\dot{\psi}_{\rm s}^{\rm r} + j\omega_{\rm r}\psi_{\rm s}^{\rm r}\right)\times \boldsymbol{I}_{\rm s}^{\rm r} \\ &= -\frac{3}{2}\left[j(\omega_1-\omega_{\rm r})\psi_{\rm s}^{\rm r} + j\omega_{\rm r}\psi_{\rm s}^{\rm r}\right]\times\left(\frac{\psi_{\rm s}^{\rm r}}{\sigma L_{\rm s}} - \frac{L_{\rm m}\psi_{\rm r}^{\rm r}}{\sigma L_{\rm s}L_{\rm r}}\right) \\ &= -\frac{3}{2}\left(j\omega_1\psi_{\rm s}^{\rm r}\right)\times\left(\frac{\psi_{\rm s}^{\rm r}}{\sigma L_{\rm s}} - \frac{L_{\rm m}\psi_{\rm r}^{\rm r}}{\sigma L_{\rm s}L_{\rm r}}\right) \\ &= \frac{3}{2}\frac{\omega_1}{\sigma L_{\rm s}}\left[\left(j\psi_{\rm s}^{\rm r}\right)\times\left(\frac{L_{\rm m}}{L_{\rm r}}\psi_{\rm r}^{\rm r} - \psi_{\rm s}^{\rm r}\right)\right] \end{aligned} \tag{A3}$$

Taking into account Fig. 3, (7a) and (7b), the above equation can be expressed as

$$Q_{\rm s} = \frac{3}{2}\frac{\omega_1}{\sigma L_{\rm s}}\left|\psi_{\rm s}^{\rm r}\right|\left(\frac{L_{\rm m}}{L_{\rm r}}\left|\psi_{\rm r}^{\rm r}\right|\cos\theta - \left|\psi_{\rm s}^{\rm r}\right|\right) \tag{A4}$$

TABLE III
PARAMETERS OF THE DFIG SIMULATED

Rated power	2MW
Stator voltage	690V
Stator/rotor turns ratio	0.3
R_s	0.0108pu
R_r	0.0121pu (referred to the stator)
L_m	3.362pu
$L_{\sigma s}$	0.102pu
$L_{\sigma r}$	0.11pu (referred to the stator)
Lumped inertia constant	0.5
Number of pole pairs	2

APPENDIX B

PARAMETERS OF THE DFIG USED FOR SIMULATION

See Table III.

ACKNOWLEDGMENT

The authors are grateful to Areva T&D Ltd. Power Electronic Systems for giving permission to publish this paper.

REFERENCES

[1] S. Muller, M. Deicke, and R. W. De Doncker, "Doubly fed induction generator systems for wind turbines," *IEEE Ind. Appl. Mag.*, vol. 17, no. 1, pp. 26–33, May–Jun. 2002.
[2] H. Akagi and H. Sato, "Control and performance of a doubly-fed induction machine intended for a flywheel energy storage system," *IEEE Trans. Power Electron.*, vol. 17, no. 1, pp. 109–116, Jan. 2002.
[3] R. Pena, J. C. Clare, and G. M. Asher, "Double fed induction generator using back-to-back PWM converter and its application to variable-speed wind-energy generation," *Proc. IEE B Electr. Power Appl.*, vol. 143, no. 3, pp. 231–241, May 1996.
[4] I. Takahashi and T. Noguchi, "A new quick-response and high-efficiency control strategy of an induction motor," *IEEE Trans. Ind. Appl.*, vol. IA-22, no. 5, pp. 820–827, Sep.–Oct. 1986.
[5] M. Depenbrock, "Direct self control of inverter-fed induction machines," *IEEE Trans. Power Electron.*, vol. 3, no. 5, pp. 420–429, Oct. 1989.
[6] G. S. Buja and M. P. Kazmierkowski, "Direct torque control of PWM inverter-fed AC motors—A survey," *IEEE Trans. Ind. Electron.*, vol. 51, no. 4, pp. 744–757, Aug. 2004.
[7] M. P. Kazmierkowski and A. Kasprowicz, "Improved direct torque and flux vector control of PWM inverter-fed induction motor drives," *IEEE Trans. Ind. Electron.*, vol. 42, no. 4, pp. 344–350, Aug. 1995.
[8] P. Vas, *Sensorles Vector and Direct Torque Control*. Oxford, U.K.: Clarendon, 1998.
[9] U. Baader, M. Depenbrock, and G. Gierse, "Direct self control (DSC) of inverter-fed induction machine—A basis for speed control without speed measurement," *IEEE Trans. Ind. Appl.*, vol. 28, no. 3, pp. 581–588, May–Jun. 1992.
[10] L. Zhong, M. F. Rahman, W. Y. Hu, and K. W. Lim, "Analysis of direct torque control in permanent magnet synchronous motor drives," *IEEE Trans. Power Electron.*, vol. 12, no. 3, pp. 528–536, May 1998.
[11] A. D. Cheok and Y. Fukuda, "A new torque and flux control method for switched reluctance motor drives," *IEEE Trans. Power Electron.*, vol. 17, no. 4, pp. 543–557, Jul. 2002.
[12] T. Noguchi, H. Tomiki, S. Kondo, and I. Takahashi, "Direct power control of PWM converter without power-source voltage sensors," *IEEE Trans. Ind. Appl.*, vol. 34, no. 3, pp. 473–479, May–Jun. 1998.
[13] M. Malinowski, M. P. Kazmierkowski, S. Hansen, F. Blaabjerg, and G. D. Marques, "Virtual-flux-based direct power control of three-phase PWM rectifiers," *IEEE Trans. Ind. Appl.*, vol. 37, no. 4, pp. 1019–1027, Jul.–Aug. 2001.
[14] G. Escobar, A. M. Stankovic, J. M. Carrasco, E. Galvan, and R. Ortega, "Analysis and design of direct power control (DPC) for a three phase synchronous rectifier via output regulation subspaces," *IEEE Trans. Power Electron.*, vol. 18, no. 3, pp. 823–830, May 2003.
[15] K. P. Gokhale, D. W. Karraker, and S. J. Heikkila, "Controller for a wound rotor slip ring induction machine," U.S. Patent, 6448735B1, Jul. 22, 2002.
[16] H. W. Van Der Broeck, H. C. Skudelny, and G.V. Stanke, "Analysis and realization of a pulsewidth modulator based on voltage space vectors," *IEEE Trans. Ind. Appl.*, vol. 24, no. 1, pp. 142–150, Jan.–Feb. 1988.
[17] Y. Murai, K. Ohashi, and I. Hosono, "New PWM method for fully digitized inverters," *IEEE Trans. Ind. Appl.*, vol. 23, no. 5, pp. 887–893, Sep.–Oct. 1987.
[18] J. L. Thomas, S. Poullain, and A. Benchaib, "Analysis of a robust DC-bus voltage control system for a VSC-transmission scheme," in *Proc. IEE 7th Int. Conf. AC-DC Power Transmission*, Nov. 28–30, 2001, pp. 119–124.
[19] L. Xu and V. G. Agelidis, "Flying capacitor multilevel PWM converter based UPFC," *Proc. Inst. Elect. Eng. B*, vol. 149, no. 4, pp. 304–310, Jul. 2002.
[20] T. G. Habetler, F. Profumo, M. Pastorelli, and L. M. Tolbert, "Direct torque control of induction motor using space vector modulation," *IEEE Trans. Ind. Appl.*, vol. 28, no. 5, pp. 1045–1053, Sep.–Oct. 1992.

Lie Xu (M'03–SM'06) received the B.Sc. degree from Zhejiang University, Hangzhou, China, in 1993, and the Ph.D. degree from the University of Sheffield, Sheffield, U.K., in 1999, both in electrical and electronic engineering.

From 1999 to 2000, he was with the Centre for Economic Renewable Power Delivery (CERPD), University of Glasgow, Glasgow, U.K. After this, he was with ALSTOM T&D, Stafford, U.K. for three years. Currently, he is a Lecturer with the School of Electronic, Electrical Engineering and Computer Science, Queen's University of Belfast, Belfast, U.K. His current research interests include power electronics, renewable energy, and application of power electronics to power systems.

Phillip Cartwright received the B.Eng. (Hons.) degree from Staffordshire University, Stafford, U.K., in 1995, and the Ph.D. degree from the University of Manchester Institute of Science and Technology (UMIST), Manchester, Derby, U.K., in 2004, both in electrical engineering.

Currently, he is Head of electrical systems at Rolls-Royce plc, U.K. working in civil aerospace, defence, marine and energy related systems. He started his career in the design of high voltage direct current (HVDC) schemes. He has since designed control systems for several power system applications including HVDC, flexible ac transmission systems and doubly fed induction generator-based wind turbines. He was previously a prominent consultant with AREVA, working with developers, wind turbine manufacturers, and network operators throughout the world—and has a reference of numerous successful projects from feasibility study through to system implementation. In addition to systems level applications for renewable energy, his research interests are now with power electronics and power dense machines for more electric aircraft and land based vehicles. He is also a Visiting Lecturer at The University of Manchester (formerly UMIST).

Dr. Cartwright is a Chartered Engineer, a member of the IEE PN Executive and an Active Member of both CIGRE WG B4-39 and C6-08.